

Interconversion-controlled liquid-liquid phase separation in a molecular chiral model

Cite as: J. Chem. Phys. 155, 204502 (2021); doi: 10.1063/5.0071988

Submitted: 18 September 2021 • Accepted: 31 October 2021 •

Published Online: 22 November 2021



View Online



Export Citation



CrossMark

Betul Uralcan,^{1,a}  Thomas J. Longo,²  Mikhail A. Anisimov,^{2,3}  Frank H. Stillinger,⁴  and Pablo G. Debenedetti^{1,b} 

AFFILIATIONS

¹ Department of Chemical and Biological Engineering, Princeton University, Princeton, New Jersey 08544, USA

² Institute for Physical Science and Technology, University of Maryland, College Park, Maryland 20742, USA

³ Department of Chemical and Biomolecular Engineering, University of Maryland, College Park, Maryland 20742, USA

⁴ Department of Chemistry, Princeton University, Princeton, New Jersey 08544, USA

^aCurrent address: Department of Chemical Engineering and Polymer Research Center, Bogazici University, Bebek 34342, Istanbul, Turkey.

^bAuthor to whom correspondence should be addressed: pdebene@princeton.edu

ABSTRACT

Liquid–liquid phase separation of fluids exhibiting interconversion between alternative states has been proposed as an underlying mechanism for fluid polyamorphism and may be of relevance to the protein function and intracellular organization. However, molecular-level insight into the interplay between competing forces that can drive or restrict phase separation in interconverting fluids remains elusive. Here, we utilize an off-lattice model of enantiomers with tunable chiral interconversion and interaction properties to elucidate the physics underlying the stabilization and tunability of phase separation in fluids with interconverting states. We show that introducing an imbalance in the intermolecular forces between two enantiomers results in nonequilibrium, arrested phase separation into microdomains. We also find that in the equilibrium case, when all interaction forces are conservative, the growth of the phase domain is restricted only by the system size. In this case, we observe phase amplification, in which one of the two alternative phases grows at the expense of the other. These findings provide novel insights on how the interplay between dynamics and thermodynamics defines the equilibrium and steady-state morphologies of phase transitions in fluids with interconverting molecular or supramolecular states.

Published under an exclusive license by AIP Publishing. <https://doi.org/10.1063/5.0071988>

I. INTRODUCTION

Chirality is ubiquitous in nature, and understanding how chiral molecules interact and self-assemble is important to fundamental problems in chemistry, biology, and physics as well as for practical applications.^{1–4}

Many biological systems are chiral at different levels of organization, including the monomers that constitute proteins, nucleic acids, and membranes, as well as the mesoscopic and macroscopic structures that they form, such as the DNA double helix, plant tendril helices, and human appendages.^{2,3} From a practical point of view, chirality also plays a key role in many industrial processes.^{5–7} The active ingredients of many drugs are chiral molecules, and their different enantiomers can exhibit significant differences in activity, absorption, selectivity, and toxicology.^{8–10} In addition, engineering

the chirality of inorganic materials has recently attracted a great deal of attention in chiral sensing, catalysis, and advanced optical device technologies.^{11–13} Molecular level insight on chiral preference and phase behavior is thus desirable to guide synthesis and processing techniques for this rich array of potential technological applications.

While chiral molecules are commonly synthesized as racemic mixtures (equal proportions of both enantiomers), the molecules of life are comprised of asymmetric building blocks composed of only one of the two possible enantiomers of a given chiral pair (e.g., L-amino acids in proteins and D-deoxyribose in nucleic acids).^{1,2} This is a distinguishing feature of life. Consequently, chiral symmetry preferences found in nature have long been a subject of investigation.^{2,14–24} While many studies have yielded useful insights, the question of how biological homochirality arose in nature, including whether it was predefined or random, remains an area of much

TABLE I. Parameters for the chiral model.^a

| | k_s | k_b | k_d | b |
|---------|-----------------------------|--------------|---------------------|--------|
| Actual | 196 kcal/mol Å ² | 193 kcal/mol | 0.003–7.76 kcal/mol | 3.7 Å |
| Reduced | 8003 | 643.7 | 0.001–25.86 | 1.0583 |

^aThroughout the paper, distances are expressed in units of $\sigma_{tt} = 3.5 \text{ \AA}$ [see Eq. (3)], energies in units of $\epsilon_0 = 0.3 \text{ kcal/mol}$ [see Eq. (4)], temperatures in units of $\epsilon_0/k = 150.9 \text{ K}$ (k is Boltzmann's constant), pressures in units of $\epsilon_0\sigma_{tt}^{-3} = 486 \text{ bars}$, densities in units of $\sigma_{tt}^{-3} = 0.023 \text{ \AA}^{-3}$, and time in units of $\sigma_{tt}\sqrt{m^*/\epsilon_0} = 0.3124 \text{ ps}$, where $m^* = 1 \text{ g/mol}$. The mass of a monomer was set to $8.5m^*$, yielding a molecular weight of 34 g/mol.

current activity.^{25–33} Studies of the origin of biological homochirality often involve the search for common principles that seek to explain how a small chiral imbalance can be amplified and subsequently transmitted, giving rise to symmetry breaking.³ In this regard, gaining a fundamental understanding of systems where the chirality of a single molecule influences the phase behavior at larger length scales is of significant importance.

Chiral states are not static in nature, and often the individual molecules of different chiralities may interconvert. Interconversion between alternative molecular states of systems exhibiting phase separation is a ubiquitous phenomenon that has been previously found in many condensed matter systems.^{34–47} In this work, we study the interplay between chiral interconversion kinetics and phase behavior in the liquid phase of a three-dimensional, off-lattice, flexible tetramer model.⁴⁸ This model consists of chiral tetramer molecules with a tunable interconversion rate between the two enantiomeric forms. It also includes a pair potential energy function with a tunable chiral bias parameter that can favor either locally racemic or heterochiral interactions. We consider two formulations of the chiral model—one with energy conservation and another one with energy dissipation.

The conserved-force formulation was introduced recently by Petsev *et al.*,⁴⁹ but we use different numerical values for the model parameters (see Table I). In equilibrium, when all interaction forces are balanced, the growth of the phase domain is restricted only by the size of the system. In this case, we observe the phenomenon of phase amplification (phase bullying), in which one of the two alternative phases grows at the expense of the other.^{48,50} The dissipative formulation considers an imbalance of intermolecular forces resulting from not applying the gradient operator to the chirality-dependent term in the potential energy function.⁴⁸ It corresponds to a nonequilibrium system, in which the imbalance in intermolecular forces facilitates racemization. This racemizing force competes with the equilibrium interconversion and diffusion. At infinite times, this competition leads to the formation of steady-state arrested microphase domains.

The rest of this paper is organized as follows. In Sec. II, we describe the tetramer model and introduce the model parameters that we use to tune chiral interactions and interconversion kinetics. In Secs. III A and III B, we discuss our results on the conserved and dissipative force formulations of the chiral model, respectively. We show how the interplay between spinodal decomposition and interconversion affects phase separation behavior in the two formulations of the chiral model. In Sec. IV, we provide concluding remarks and suggest some possible directions for future inquiry. Appendixes A–E provide the details on the theoretical description of the computational results.

II. MODEL AND METHODS

This simple chiral tetramer model, inspired by the smallest known chiral molecule in nature, hydrogen peroxide,^{51–53} was introduced by Latinwo *et al.*⁴⁸ and subsequently reformulated by introducing an additional eight-body force that produces an energy-conserving force field.⁴⁹ A tetramer of the chiral model is composed of four monomers along a three-bond backbone (Fig. 12). The instantaneous state of a tetramer is specified by the location of monomers along the backbone at r_1, r_2, r_3 , and r_4 . Specifically, molecules feature left-handed (*A*-type) and right-handed (*B*-type) configurations and achiral transition states (Fig. 12). The shape of the molecule is determined by the intramolecular potential energy function that includes contributions from bond stretching, bond angle deformation, and dihedral angle rotation and is given by

$$\Phi^{(1)}(\{\mathbf{r}_i\}) = \sum_{i=1}^3 \frac{k_s}{2} (r_{i,i+1} - b)^2 + \sum_{i=1}^2 \frac{k_b}{2} \left(\Theta_i - \frac{\pi}{2} \right)^2 + k_d \cos^2 \phi, \quad (1)$$

where $r_{i,i+1}$ is the instantaneous distance between sites i and $i+1$, b represents the equilibrium bond length, Θ_i and ϕ are the bond and dihedral angles, and k_s , k_b , and k_d are the force constants for bond stretching, angle bending, and dihedral motion, respectively. The dihedral force constant k_d controls the rigidity of the dihedral angle of a tetramer and determines the rate of interconversion between a pair of mirror image configurations. The chiral model parameters are given in Table I. The model's behavior is only a function of dimensionless (reduced) variables. The parameters in Table I are suggested physical constants for translating reduced units (e.g., $P^* = P\sigma_{tt}^3/\epsilon_0$) into actual physical quantities (e.g., $P = P^* \epsilon_0/\sigma_{tt}^3$).

In order to monitor the chirality and control the intermolecular interactions between tetramer pairs, we define a scalar chirality measure, $-1 \leq \zeta \leq 1$,

$$\zeta(\mathbf{r}_1, \mathbf{r}_2, \mathbf{r}_3, \mathbf{r}_4) = \frac{\mathbf{r}_{12} \cdot (\mathbf{r}_{23} \times \mathbf{r}_{34})}{|\mathbf{r}_{12}| |\mathbf{r}_{23}| |\mathbf{r}_{34}|}, \quad (2)$$

where, for each tetramer, the chirality of the enantiomer is determined by the sign of ζ . This measure attains its lower and upper limits for the mirror image left-handed (*A*-type) and right-handed (*B*-type) configurations and goes to zero for the achiral transition states illustrated in Fig. 12 (see Appendix A).

The model's intermolecular potential energy function between two molecules α and γ is given by

$$\Phi^{(2)}(\{\mathbf{r}_i^\alpha\}, \{\mathbf{r}_j^\gamma\}) = \sum_{i,j=1}^4 \epsilon_{tt}(\zeta^\alpha, \zeta^\gamma) v\left(\frac{|\mathbf{r}_i^\alpha - \mathbf{r}_j^\gamma|}{\sigma_{tt}}\right), \quad (3)$$

where the double sum runs over each site on each tetramer, σ_{tt} is the pair potential distance parameter that specifies the range of the site-site interactions, v is the 12-6 Lennard-Jones function, and ϵ_{tt} is the strength of the interaction energy between tetramers. The interaction energy term ϵ_{tt} can be tuned to favor/disfavor homochiral/heterochiral interactions between tetramers α and γ and is given by

$$\epsilon_{tt}(\zeta^\alpha, \zeta^\gamma) = \epsilon_0 [1 + \lambda \zeta(\mathbf{r}_{i=1,2,3,4}^\alpha) \zeta(\mathbf{r}_{i=1,2,3,4}^\gamma)], \quad (4)$$

where λ is the chirality renormalization parameter such that $\lambda < 0$ favors heterochiral interactions between tetramers α and γ (i.e., lower energy when α and γ have opposite chiralities), $\lambda > 0$ favors homochiral interactions between tetramers α and γ (i.e., lower energy when α and γ have the same chirality), and $\lambda = 0$ represents a bias-free scenario.⁴⁸ We note that while its numerical value is an adjustable model parameter, the chirality renormalization parameter effectively represents the local binding preferences of real chiral molecules. For instance, both aspartic acid and glutamic acid display homochiral bias ($\lambda > 0$) evident from their enantiopure crystal structures,⁵⁴ while both serine and histidine exhibit heterochiral bias ($\lambda < 0$) evident from their racemic crystal structures.⁵⁵

The two formulations of the chiral model differ in the forces that stem from the intermolecular potential defined in Eq. (3). In the first formulation,⁴⁸ only the Lennard-Jones force on monomers with interaction energy ϵ_{tt} is considered. However, the gradient operator that yields the forces corresponding to the pair potential defined in Eq. (3) applies rigorously to the entire argument inside the double summation. Hence, this model introduces dissipation through a non-conservative force. In the second formulation,⁴⁹ the gradient properly operates on the Lennard-Jones and on the chirality-dependent energy pre-factor, producing a coarse-grained energy-conserving force field. That both models are coarse-grained follows from the fact that the interaction energy between two tetramers depends explicitly on their respective chiralities, a tetramer-level (as opposed to site-level) quantity.

III. RESULTS AND DISCUSSION

Computational results for the two formulations of the chiral model, with conservative and dissipative intermolecular forces, are presented in this section. The time evolution of both formulations is described based on a generalized Cahn-Hilliard theoretical model of phase separation, which includes the molecular interconversion of species. The model is a mean field approach, which is accurate away from the critical point.

A. Chiral model with conservative intermolecular forces

In Fig. 1, the time dependence of the dihedral angle of a single tetramer in a racemic mixture of 1000 tetramers, at different temperatures and for a range of values of the dihedral force constant, is shown for the chiral model with conservative forces. It can be

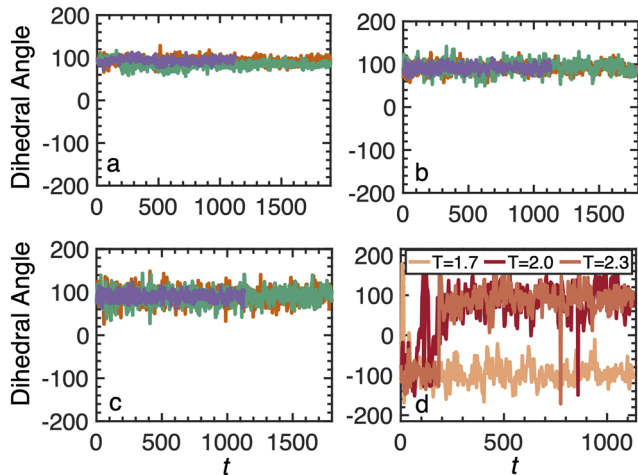


FIG. 1. Time dependence of the instantaneous dihedral angle of a typical tetramer in a racemic mixture at $P = 0.1$ for the conservative-force formulation of the model, at several values of T and k_d . (a) $T = 0.6$, (b) $T = 1.7$, and (c) $T = 2.3$, with $k_d = 5$ (green), $k_d = 9.86$ (orange), and $k_d = 19.86$ (purple). (d) Behavior of the dihedral angle at a very low value of the dihedral constant, $k_d = 0.001$.

seen that the enantiomers do not interconvert within the simulation times sampled here [Figs. 1(a)–1(c)]. Interconversion between the two enantiomorphs is achieved only at much lower k_d values [$k_d = 0.001$ in Fig. 1(d)].

When a binary mixture with equal concentrations of interconverting molecules is quenched from a high temperature to a low temperature, below the critical temperature of demixing, there are two processes that may occur. Either the system may phase separate, through a process known as spinodal decomposition,⁵⁶ or one of the two alternative phases will grow at the expense of the other, a process known as phase amplification.⁵⁰ The chiral model with conservative intermolecular forces always undergoes phase amplification below the critical demixing temperature. This is because in a system where molecules can interconvert, the number of molecules of each type (chirally distinct enantiomers in the present case) is not a conserved quantity, and hence, the system minimizes its free energy by avoiding the energetic penalty associated with the formation of an interface, and one of the two alternative phases grows at the expense of the other. Which of the two phases grows is of course a stochastic event.

The above considerations apply strictly only at true thermodynamic equilibrium. From a numerical point of view, it is important to understand that the “stiffness” of the force constant for the dihedral angle, k_d , determines the ease with which such equilibrium can be attained. The mean frequency with which an individual molecule is able to switch its chirality varies in the opposite direction to any k_d variation. Thus, below the critical temperature for demixing, and for small enough values of k_d , interconversion occurs frequently and the system is able to attain true equilibrium, resulting in phase amplification. On the other hand, for sufficiently large values of k_d , interconversion is increasingly rare, the system is under diffusive control, and phase separation, rather than amplification, occurs on practical time scales accessible to simulation, even if the system is under the action of conservative forces.

The mixed diffusion and interconversion dynamics of the chiral model can be described through a Cahn–Hilliard theoretical model of phase separation, which includes interconversion between species.⁵⁰ According to this model, the dynamics of such a system is characterized by a growth rate (see Appendix B 1 and Ref. 57) of the form

$$\omega(q) = -\Delta T(LR_0^2 + Mq^2)(1 - \xi^2 q^2), \quad (5)$$

where q is the wave number ($=2\pi/r$), R_0 is the size of the tetramer (adopted here as $R_0 = 1$ in reduced units), $\Delta T = T/T_c - 1$ is the distance to the critical temperature of demixing (negative when the system is in the unstable region), and M and L are the diffusion and interconversion Onsager kinetic coefficients, respectively. ξ^2 is the square of the correlation length of mesoscopic concentration fluctuations, which diverge at the spinodal as $\xi^2 \sim 1/(-\Delta T)$, in the mean field approximation. The self-diffusion (mobility) coefficient is given by $M \approx kT/6\pi\eta R_0$ (where η is the shear viscosity). The interconversion Onsager kinetic coefficient, L , depends on the strength of the rigidity spring constant, k_d , such that it becomes zero in the limit when $k_d \rightarrow \infty$ and diverges when $k_d \rightarrow 0$. Therefore, for large values of k_d ($M \gg L$), phase separation is expected, while for very small values of k_d ($L \gg M$), phase amplification is predicted.

Figure 2 shows the phase diagram of the chiral model in the case when $k_d = 0.001$ ($L \gg M$) and interconversion dynamics controls the phase behavior of the system. The pressure dependence of the critical temperature is empirically described by

$$T_c(P) = T_c(P=0) + \frac{\alpha P}{1+P}, \quad (6)$$

where $T_c(P=0) = 2.19$ and $\alpha = 2.43$. We point out that although k_d primarily determines the interconversion rate, it also affects the system's equilibrium thermodynamics. For example, the total pair interaction energy shows a small but non-zero dependence on k_d at otherwise identical thermodynamic conditions (Appendix C). Accordingly, one expects the critical temperature to depend on k_d . This effect is at the limit of detectability, and for numerical purposes,

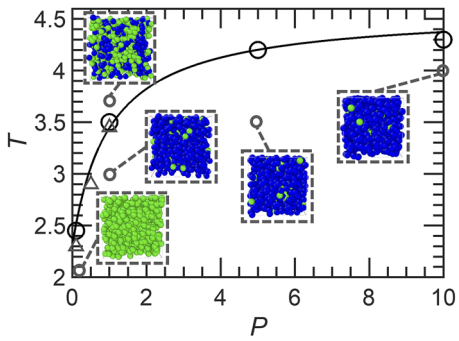


FIG. 2. Phase diagram showing chiral phase amplification for the chiral model with conservative intermolecular forces, heterochiral bias parameter $\lambda = 0.5$, and rigidity spring constant $k_d = 0.001$. The circles on the solid curve are the computational data for the critical temperature of equilibrium phase separation, and the curve is the fit of Eq. (6). The images show the snapshots of the equilibrium states for the pressures $P = 0.1$, $P = 1$, $P = 5$, and $P = 10$ below the critical temperature and at $P = 1$ above the critical temperature. The triangles show the prediction of the critical temperature from the extrapolation of the chiral model with dissipative intermolecular forces to the limit $k_d \rightarrow \infty$ (see Sec. III B).

k_d can be considered as controlling interconversion kinetics while having at most a modest effect on the system's thermodynamics.

As shown in **Fig. 2**, where $\lambda = 0.5$, above the critical temperature, a homogeneous mixture of A- and B-enantiomers is observed throughout the simulation box. The apparent mesoscopic inhomogeneities shown by the snapshot in **Fig. 2** the critical temperature are attributed to the growing correlation length of concentration fluctuations in the critical region. Below T_c , phase amplification, in which one phase grows at the expense of the other, occurs. Note that by quenching the racemic mixture below T_c , due to the effect of phase amplification,⁵⁰ the system equilibrates arbitrarily to either A- or B-type enriched enantiomer phases as illustrated in **Fig. 2**, thereby establishing a chiral preference.

B. Chiral model with dissipative intermolecular forces

Dissipative intermolecular forces prevent the chiral model from relaxing to an equilibrium state; instead, this system evolves into a nonequilibrium steady state. This effect can be accounted for by a modification in the growth rate formula, Eq. (5), where the energy dissipation causes forced racemization of species. This forced racemization competes with the inherent equilibrium interconversion.

We first studied the phase behavior of the dissipative chiral model in the absence of an explicit energetic bias for homochiral interactions ($\lambda = 0$). **Figure 3** shows the pairwise tetramer–tetramer center of mass radial distribution profiles $g(r)$ for a bias-free system of 1000 tetramers at $t = 10^6$ after starting from a homogeneous racemic configuration. While complete phase separation is not observed on the time scale of the simulations, the partial radial distribution profiles illustrate the spontaneous enhancement of homochiral interactions in the tetramer model at $P = 10$ and $T = 1.2$, illustrated by the sharp first peaks of $g(r)$ profiles for A–A and B–B tetramer pairs. Nevertheless, without an explicit bias parameter, the enhancement of homochiral interactions is observed only at very high pressures and low temperatures, where diffusion and chiral interconversion kinetics are slow. Consequently, in this study, we employ a homochiral bias parameter that energetically favors homochiral interactions ($\lambda = 0.5$) to study the liquid–liquid phase separation (LLPS) of the chiral system.

Figure 4(a) depicts the strong k_d dependence of chiral interconversion kinetics by showing the temporal evolution of the dihedral

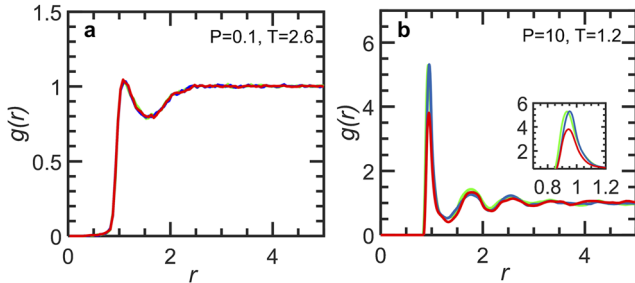


FIG. 3. Pairwise local structure in the absence of an explicit energetic bias at $k_d = 25.86$ for the dissipative-force formulation of the chiral model. Tetramer–tetramer center of mass radial distribution functions for A–A (green), B–B (blue), and A–B (red) pairs indicate (a) mixing at low pressure ($P = 0.1$) and high temperature ($T = 2.6$) and (b) local homochiral bias at high pressure ($P = 10$) and low temperature ($T = 1.2$). The inset shows the overlap between the green and blue curves.

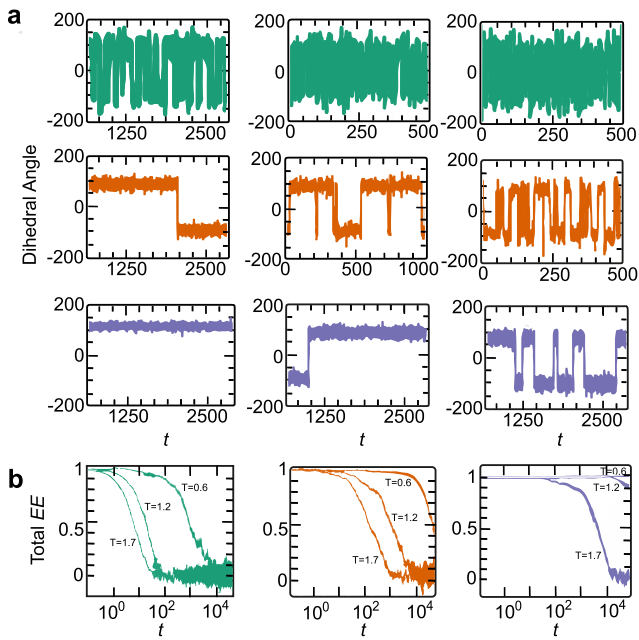


FIG. 4. Interconversion and racemization kinetics of the dissipative-force formulation of the chiral model. Temporal evolution of (a) a single tetramer in a racemic mixture, with dihedral force constant (from top to bottom) $k_d = 5$ (green), $k_d = 9.86$ (orange), and $k_d = 19.86$ (purple) at $P = 0.1$, T (left to right) = 0.6, 1.2, and 1.7 and (b) the total enantiomeric excess [see Eq. (7)] of an initially enantiopure system, with dihedral force constant (from left to right) $k_d = 5$ (green), $k_d = 9.86$ (orange) and $k_d = 19.86$ (purple) at $P = 0.1$ and $T = 0.6$, 1.2, and 1.7.

angle of a single tetramer in a racemic mixture of 1000 tetramers. At high k_d and low T , the tetramer persists longer in the vicinity of the stable enantiomorphs ($\phi \approx -90^\circ$ for A-type and $\phi \approx 90^\circ$ for B-type tetramers). In particular at $k_d = 19.86$ and $T = 0.6$, it reaches the limit at which no interconversion is observed within the simulation time (τ_{obs}). In this limit of slow interconversion, where the characteristic interconversion time of a tetramer τ_{INC} , defined as the average time required for a tetramer to switch chirality, is much longer than the total simulation time τ_{obs} , the system behaves thermodynamically as a binary mixture of enantiomers that do not interconvert. In contrast, at low k_d and high T , the tetramer interconverts between its two stable enantiomorphs very rapidly. At these conditions, the achiral transition states ($\phi \sim -180^\circ, 0^\circ, 180^\circ$ for *cis* and *trans* configurations, respectively) also become more accessible. In this opposite limit of very fast interconversion, the system can be treated thermodynamically as a single-component fluid since the characteristic interconversion time τ_{INC} is much shorter than the total simulation time τ_{obs} .

Comparing the interconversion kinetics of the dissipative force formulation of the chiral model [Fig. 4(a)] with the conservative force formulation (Fig. 1), one can see that dissipation lowers the barrier to enantiomer racemization, thereby causing the chiral interconversion rate to increase. The increase in the interconversion kinetics in the dissipative formulation reflects the absence of the additional force contribution arising, in the conservative case, from applying the spatial gradient operator to the chirality-dependent characteristic energy ϵ_{tt} .

Next, to investigate the effect of the interconversion rate on the racemization kinetics, we study the time-dependent behavior of the average chirality [the total enantiomeric excess (EE)] of the tetramer system, starting from an enantiopure configuration [Fig. 4(b)]. The total enantiomeric excess (EE) for the bulk tetramer system is defined by

$$\text{Total EE} = \frac{N_A - N_B}{N_A + N_B}, \quad (7)$$

where N_A and N_B are the number of A- and B-type tetramers, respectively. At low k_d and high T , systems that start from enantiopure configurations (total EE = 1) tend rapidly toward racemic mixtures with vanishing average chirality, consistent with the corresponding tetramer interconversion kinetics profiles. Conversely, the total EE of high k_d and low T systems remains constant within τ_{obs} , demonstrating that these systems can be treated as non-interconverting binary mixtures [Fig. 4(b)], $k_d = 19.86$ and $T = 0.6$ and 1.2.

In order to understand the growth of the spatial correlation of enantiomorphs as a function of time, we compute a time- and position-dependent order parameter $ee(r, t)$ given by

$$ee(r, t) = \frac{N_A(r, t) - N_B(r, t)}{N_A(r, t) + N_B(r, t)}. \quad (8)$$

Equation (8) applies to the case where the molecule at $r = 0$ is an A enantiomorph. If instead a B molecule is at $r = 0$, the numerator changes to $N_B(r, t) - N_A(r, t)$. This order parameter is inspired by Cahn–Hilliard theory,⁵⁸ where $ee(r, t)$ defines the length scale dependent ordering process in a phase-separating binary mixture when quenched below the coexistence and spinodal lines. The physical significance of the order parameter is as follows: The order parameter approaches unity when the neighbors of an enantiomorph at a distance r are of the same type as the molecule at the origin, signifying compositional inhomogeneity (and possibly phase separation) at the length scale r . When the enantiomorphs are homogeneously mixed, $ee(r, t)$ decays to zero. We compute the spatial correlation of $ee(r, t)$ using

$$C(r, t) = \frac{\langle ee(r', t)ee(r' + r, t) \rangle - \langle ee(r', t) \rangle \langle ee(r' + r, t) \rangle}{\langle ee(r', t)ee(r', t) \rangle - \langle ee(r', t) \rangle \langle ee(r', t) \rangle}. \quad (9)$$

Figure 5 shows the temporal evolution of the $C(r, t)$ profiles for a homogeneously mixed racemic mixture of 1000 particles with $k_d = 11.86$, quenched from $T = 2.6$ to $T = 0.8$. The distance R at which $C(r, t)$ first decays to zero ($r = R$) gives the average domain size, hence the characteristic length scale of the phase separation. The two enantiomorphs A and B are marked as green and blue tetramers, respectively. Initially, the spatial correlation function $C(r, t)$ fluctuates around zero, signifying that the enantiomorphs are homogeneously mixed before the quench, $R(t = 0) = 0$. After the quench, the tetramers interconvert and diffuse in such a way that local enantiopure configurations start to be favored. At early times ($t = 150$), the correlation length R is small, indicating the formation of small enantiomorph clusters. At later stages ($t = 300$), phase separation proceeds rapidly as these small domains merge. The rapid phase separation process slows down after $t = 300$, and coarsening of the A- and B-rich phases takes over. This final stage completes when the

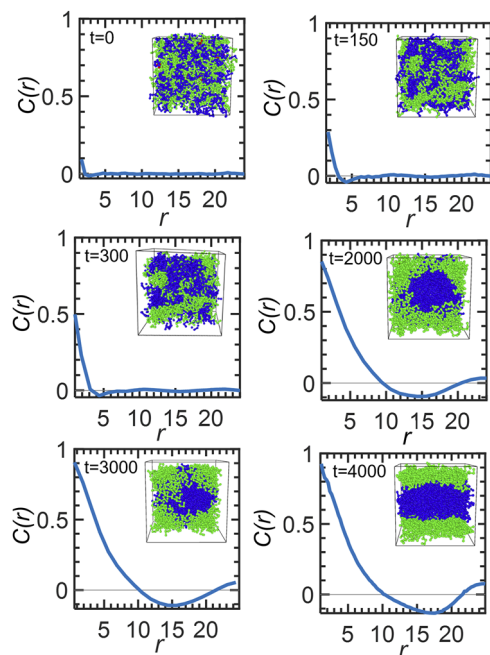


FIG. 5. Phase separation kinetics of the dissipative-force formulation of the chiral model. Temporal evolution of phase separation depicted by the instantaneous spatial correlation profiles and representative snapshots for a racemic mixture ($k_d = 9.86$, $T = 0.8$, and $P = 0.1$).

rough edges of the interface between the two enantiomorph phases are smoothed ($t = 4000$).

In Fig. 6, we illustrate kinetically arrested liquid–liquid phase separation for the dissipative-force formulation of the chiral model at the scale of the simulation system (wave number, $q = 2\pi/\ell$, where ℓ is the length of the simulation box). In particular, starting from a homogeneous racemic mixture of enantiomers, we study the steady-state behavior of the tetramer system upon quenching to a temperature and pressure of interest. Figure 6(a) shows the representative local enantiomeric excess profiles for phase-separated ($k_d = 19.86$ and $T = 1$) and homogeneously mixed systems ($k_d = 19.86$ and $T = 2$) that have reached steady-state. Figure 6(b) shows the apparent onset temperature of liquid–liquid phase separation (T^*) defined as the temperature where the growing steady-state domain size, R_∞ , reaches the size of the simulation box, $R_{\max} \sim \ell$. This temperature increases with the rigidity of the dihedral angle of the tetramers. Phase separation can be considered fully developed below the onset temperature. However, interconversion frustrates complete phase separation above the onset temperature. As illustrated by the simulation snapshots of Fig. 6(b), above T^* , we observe phase separated domains of smaller sizes $R_\infty < R_{\max}$.

The k_d dependence of the temporal evolution of an equimolar mixture of enantiomorphs as the system moves from a homogeneous mixture toward phase separation is illustrated in Figs. 7(a) and 7(b). In particular, Figs. 7(a) and 7(b) depict $R(t)$ normalized by the maximum phase separation length scale R_{\max} (i.e., when the domain growth is restricted by the finite size ℓ of the system) for short [Fig. 7(a)] and long [Fig. 7(b)] time scales. When $R(t)$ reaches

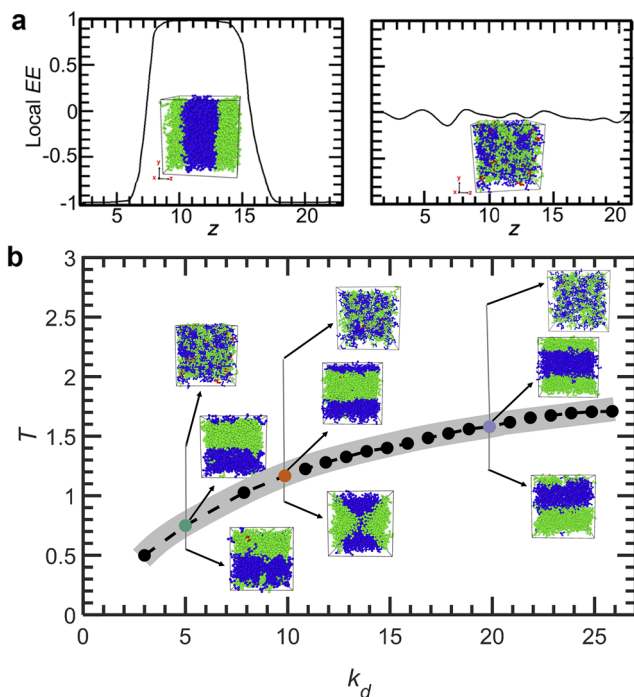


FIG. 6. Chirality-induced liquid–liquid phase separation with explicit bias that favors homochiral interactions ($\lambda = 0.5$) in the dissipative-force formulation. (a) Local enantiomeric excess profiles as a function of distance normal to the planar interface $z = 0$ for a fully phase separated system ($R_\infty = R_{\max}$) (left) and a system with small enantiomorph clusters ($R_\infty < R_{\max}$) (right). (b) Onset temperature, T^* , for liquid–liquid phase separation at the length scale of the simulation box as a function of dihedral angle force constant, k_d , at $P = 0.1$. The colored points represent the conditions for the snapshots of the chiral system above, at, and below T^* . The dashed line is given as a guide for T^* . The gray lane illustrates the uncertainty in the definition of $T^* \approx \pm 0.1$.

R_{\max} , the mixture is fully separated at the scale of the simulation box and the domains stop growing. The dashed curves indicate the theoretical prediction for the domain growth if it would not be restricted by the size of the simulation box (see below and Appendix D). At $k_d = 19.86$, corresponding to a relatively rigid dihedral angle spring constant, the time of phase separation τ_{LLPS} , defined as the time when $R(t)/R_{\max} = 1$, is about 800 [see Fig. 7(a)]. When $k_d = 9.86$, the time required for full phase separation increases to $\tau_{LLPS} = 4000$.

Figure 7(b) illustrates the infinite time limit of the dependence of the steady-state domain length, $R(t \rightarrow \infty) = R_\infty \propto k_d$, on the dihedral force constant of the tetramer model at $P = 0.1$ when the system is quenched from $T = 2.6$ to $T = 0.8$. This dependence is consistent with the result presented in the inset of Fig. 8(b), where R_∞ is depicted as proportional to k_d . It is shown that below $k_d = 25.86$, the domain growth saturates at a certain steady-state value below R_{\max} , which is shown by the smaller tetramer inhomogeneities in Fig. 8(a). The emergence of such smaller domain sizes suggests that the growth of the domains at these conditions is restricted by the dissipation in the intermolecular interaction forces, not by the finite length scale of the simulation box. As the interconversion Onsager kinetic coefficient, L , is inversely related to the characteristic time of interconversion, τ_{INC} , we note that the data can be well described

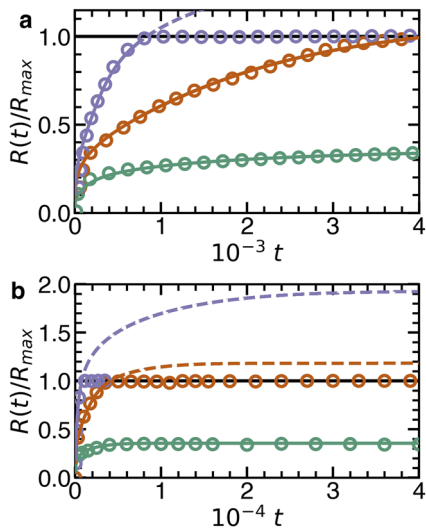


FIG. 7. Growth of the domain size $R(t)$ in the dissipative-force formulation of the chiral model (a) for short growth times and (b) long growth times for dihedral force constants $k_d = 5$ (green), $k_d = 9.86$ (orange), and $k_d = 19.86$ (purple) at $P = 0.1$ and $T = 0.8$. $R(t)/R_{\max} = 1$ corresponds to the length scale of the simulation box. The size of a phase domain is restricted by this length scale, and thus, the dashed curves correspond to predictions of the domain growth that could be observed if it would not be restricted by the size of the simulation box. The open circles are computational data, while the solid and dashed curves are obtained from the maximum of the time-dependent structure factor for the domain growth—see Appendix D and Ref. 57. The steady-state limit of the size of a phase domain, R_∞ , is proportional to the magnitude of the dihedral force constant.

by $1/\tau_{\text{INC}} = a_1/R_\infty^2 + a_2/R_\infty^4$ [solid line in Fig. 8(b)], consistent with the kinetics of the domain growth presented in Fig. 7(b). When $k_d = 25.86$, the system reaches the onset of phase separation where the enantiomers completely phase separate at the size of the simulation box upon reaching equilibrium ($R_\infty = R_{\max}$). Since $R_\infty \propto k_d$ and the interconversion rate is related to the kinetic Onsager coefficient as $L = 1/\tau_{\text{INC}}$, in which the term of order $1/R_\infty^4$ is negligible (for all $R_\infty > 1$) in the first order approximation, L is given as

$$L = \frac{1}{\tau_{\text{INC}}} \approx M \frac{T^2}{k_d^2}, \quad (10)$$

where the squared temperature dependence comes from the natural coupling between dihedral angle rotation and thermal energy in an equilibrium ensemble. Furthermore, the assumption $L \propto M$ provides a good fit to simulation data (see Fig. 8) and implies that enantiomer interconversion is linked to rotational mobility (the latter being proportional to translational mobility through the Stokes–Einstein and Debye–Stokes–Einstein equations).

The generalized Cahn–Hilliard model with interconversion of species, introduced in the discussion of Eq. (5), can be adapted to the dissipative chiral model by introducing an imbalance of chemical potentials, which produces nonequilibrium forced racemization (see Appendix B 2 and Ref. 57 for details). As a result, the form of the growth rate for the dissipative formulation of the chiral model is

$$\omega(q) = -L(\hat{T} + q^2) - M\Delta T q^2(1 - \xi^2 q^2), \quad (11)$$

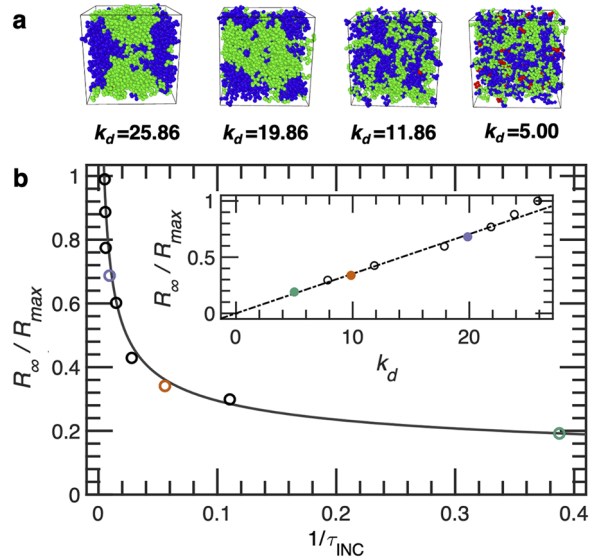


FIG. 8. Change in compositional heterogeneity with chiral interconversion kinetics at $T = 1.7$ and $P = 0.1$ in the dissipative-force formulation. (a) Steady-state snapshots of chiral liquid systems at various dihedral force constants (k_d). (b) Steady-state domain size as a function of interconversion rate, $1/\tau_{\text{INC}}$. The solid line is the approximation given by $1/\tau_{\text{INC}} = a_1/R_\infty^2 + a_2/R_\infty^4$, where $a_1 = 4.6 \times 10^{-3}$ and $a_2 = 3.8 \times 10^{-4}$. In the first-order approximation, this follows from Eqs. (10) and (12). The inset shows the linear correlation between R_∞ and k_d . The colored points highlight the results corresponding to the three dihedral force constants for which the domain growth is shown in Fig. 7.

where $\hat{T} = T/T_c$ and L is given by Eq. (10). It is seen that the only difference between Eqs. (5) and (11) is that the interconversion Onsager kinetic coefficient, L , is decoupled from ΔT . This equation is illustrated in Fig. 9, in which the effect of dissipation can be seen in the downward shift of the growth rate curve. We note that, in this form, this growth rate formula resembles the one introduced in the nonequilibrium lattice model of Glotzer *et al.*, in which forced interconversion is decoupled from equilibrium phase separation.^{43,44} Glotzer and co-workers showed that phase separation driven by spinodal decomposition can be kinetically arrested at a certain scale due to the suppression of the growth of low wave-number inhomogeneities. Our computational results for the dissipative force formulation of the chiral model confirm the assessments made by Lefever *et al.*,^{46,47} and more recently, Lamorgese and Mauri,⁴⁵ who argued that the results of Glotzer *et al.*^{43,44} are limited to nonequilibrium conditions, where a source of forced interconversion, which inhibits the relaxation of the system to equilibrium, leads to the steady-state phenomenon of arrested phase separation into microdomains.

One can predict the size of the steady-state arrested domains from the condition that the growth rate becomes zero at a nonzero wave number, q_- ,⁵⁷ which is inversely proportional to the size of the domain, $q_- \propto 1/R_\infty$. Solving Eq. (11) for this wave number in the first order approximation ($T^2/k_d^2 \ll 1$) gives

$$q_-^2 = \frac{L}{-D_{\text{eff}}} \approx \frac{T^2}{k_d^2(-\Delta\hat{T})}, \quad (12)$$

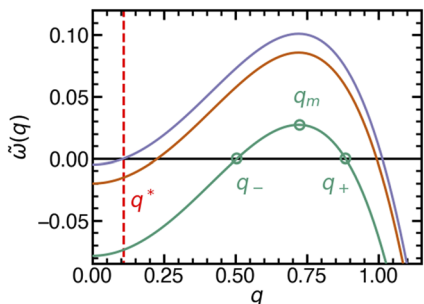


FIG. 9. Growth rate, given by Eq. (11), at constant temperature for dihedral force constants: $k_d = 5$ (green), $k_d = 9.86$ (orange), and $k_d = 19.86$ (purple), where $T = 1.8$, $T_c = 2.3$, $M = 0.8$, and L is calculated from Eq. (10). The red-dashed line corresponds to the inverse maximum size of the phase domain $1/R_{\max} \approx q^* \sim 1/\ell$. Here, we adopt $q^* = 0.11$ as obtained from the onset of phase separation on the length scale of the simulation box. The existence of a non-zero $q_- > q^*$ indicates the formation of steady-state microdomains.

where $D_{\text{eff}} = (M\Delta T + L)/\hat{T}$ is the effective mutual diffusion coefficient and $\Delta\hat{T} = \Delta T/\hat{T} = 1 - T_c/T$. Indeed, as shown in the steady-state limit of Fig. 7(b) and in the inset of Fig. 8(b), R_∞ is proportional to k_d as predicted by Eq. (12). Equation (12) illustrates the physics of microphase separation: the competition between racemization and negative diffusion.

Within our simulations, we observed a finite size effect, in which the small size of the simulation box limited the size of the steady-state microdomains, such that, computationally, it would appear as if complete phase separation was occurring. Such an effect may also be predicted from the growth rate formula and characteristic size, Eqs. (11) and (12). For certain temperatures (at constant k_d), the characteristic wavelength, q_- , reaches the characteristic wavelength of the simulation box, q^* (which is related to the size of the simulation box through $R_{\max} \sim 1/q^*$); hence, phase separation is observed on the length scale of the computation box. Since q_- is cut off at q^* , the temperature corresponding to the cutoff (T^*) characterizes the onset of the observed phase separation. The effect of this cutoff is consistent with what is illustrated in Fig. 7(b), where (for $k_d = 9.86$ and $k_d = 19.86$) the computational data show that the steady-state domain size stops growing when the system reaches the size of the simulation box.

In order to further elucidate the kinetics of phase separation, we next consider the correlations between the characteristic interconversion time of a tetramer τ_{INC} , the characteristic phase separation time τ_{LLPS} , and the characteristic molecular self-diffusion time τ_D , given by

$$\tau_D = \frac{R_0^2}{D_{\text{eff}}}, \quad (13)$$

where R_0 is the radius of the tetramer's first solvation shell based on the site-site radial distribution function and D_{eff} is the effective (k_d -dependent) self-diffusion coefficient computed from the slope of the time dependence of the mean-square displacement of all tetramers in the simulation box (Fig. 10). The circles correspond to temperatures below the onset of phase separation. Figure 10 demonstrates a strong coupling between the characteristic time of molecular diffusivity τ_D , the characteristic time of phase separation τ_{LLPS} , and the characteristic time of interconversion τ_{INC} .

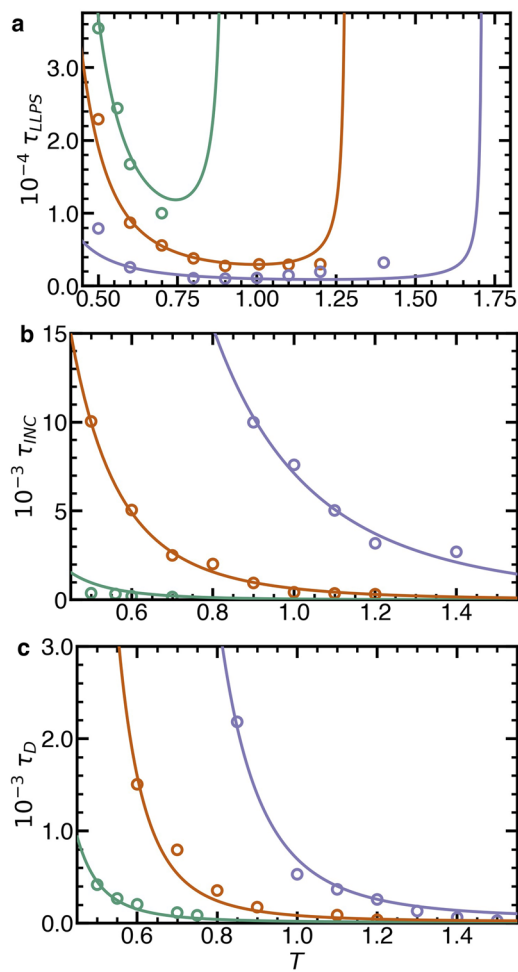


FIG. 10. Temperature dependence of the characteristic time scales in the dissipative-force formulation of the chiral model for dihedral force constants: $k_d = 5$ (green), $k_d = 9.86$ (orange), and $k_d = 19.86$ (purple) at $P = 0.1$. (a) Characteristic time for liquid–liquid phase separation at the length scale of the simulation box, $q = q^*$. The curves are $\tau_{\text{LLPS}} \propto 1/\bar{\omega}(q^*)$, where $\bar{\omega}(q)$ is given by Eq. (11) where it was found that $q^* = 0.15$ and $T_c = 2.35$. The condition $\tau_{\text{LLPS}} \rightarrow \infty$ corresponds to $T = T^*$. (b) Characteristic times for chiral interconversion. $\tau_{\text{INC}} \propto 1/L$, and the curves are given by Eq. (E1). (c) Characteristic self-diffusion times, and the curves are given by Eq. (14). The parameters of Eqs. (11), (E1), and (14) used for the fits are given in Appendix E.

In the two phase region, the growth rate formula, Eq. (11), describes the characteristic times of liquid–liquid phase separation (LLPS) on the length scale of the simulation box. As seen in Fig. 10(a), the time of LLPS becomes infinite when the microdomain sizes reach the size of the simulation box, $q_- = q^*$. As indicated in Fig. 10, this scenario corresponds to $T = T^*$. The time of LLPS affected by interconversion is defined through Eq. (11) as $\tau_{\text{LLPS}} = a_{\text{LLPS}}/\bar{\omega}(q^*)$, where the amplitude $a_{\text{LLPS}} = 0.34$, in the region where $q_- < q^*$ (or, equivalently, where $R_\infty > \ell$) as illustrated in Fig. 10(a) (see Appendix E for details).

The interconversion time in the two phase region ($T < T^*$), as shown in Fig. 10(b), is well-described by the extended version of

Eq. (10) [Eq. (E1)] in which the next order, k_d^4 term, is included. In addition, the self-diffusion coefficient affected by interconversion is theoretically predicted from the coefficient of q^2 in $\hat{\omega}(q)$ as given by Eq. (B8) (see also Appendix E) such that the effective diffusion coefficient $D_{\text{eff}} = (M\Delta T + L)/\hat{T}$, and Eq. (13) reads

$$\tau_D = \frac{R_0^2}{(M\Delta T + L)/\hat{T}}. \quad (14)$$

The self-diffusion time shown in Fig. 10(c) exhibits a crossover from the inverse mobility, $\tau_D \propto \hat{T}/M\Delta T$ (at large k_d), to the interconversion time, $\tau_D \propto \hat{T}/L$ (at small k_d).

The asymptotic limit of τ_{LLPS} indicates the onset temperature, T^* , where phase separation occurs on the length scale of the simulation box. The onset temperature as a function of dihedral angle force constant, k_d , is depicted in Fig. 11(a). The onset temperature is numerically calculated from $\omega(q = q^*) = 0$, given by Eq. (11). In the first order approximation, this solution is given by Eq. (12) if $q_- = q^*$ and $T = T^*$. As depicted in Fig. 11(a), the onset of arrested phase separation on the scale of the simulation box also depends on pressure. Physically, this originates from the density-dependent energetic bias toward homochiral interactions (Fig. 3), represented phenomenologically by the introduction of $\lambda > 0$ in the model. Thermodynamically, this pressure dependence of T^* can be attributed to

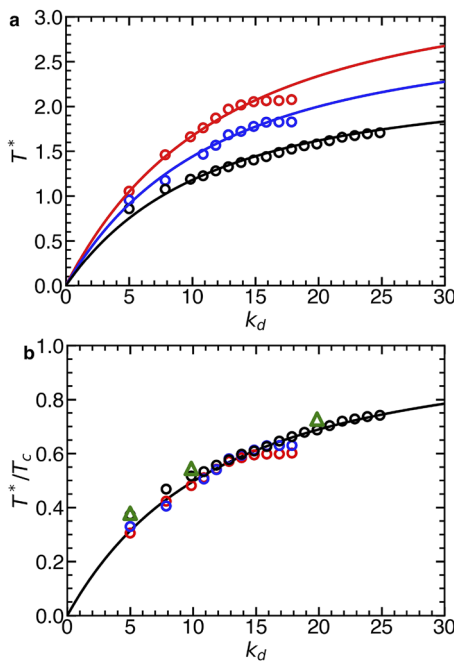


FIG. 11. Dihedral force constant dependence of the onset temperature of phase separation on the length scale of the simulation box in the dissipative-force formulation chiral model for $P = 1.0$ (red circles), $P = 0.5$ (blue circles), and $P = 0.1$ (black circles). The curves are numerically calculated from the first solution of $\hat{\omega} = 0$, given by Eq. (11), when $q_- = q^* = 0.11 \approx 1/R_{\max} \sim 1/\ell$, $T = T^*$, and $T_c(P = 1.0) = 3.45$, $T_c(P = 0.5) = 2.91$, and $T_c(P = 0.1) = 2.3$ for different pressures (a) and in rescaled coordinates (b). The triangles, shown in (b), are obtained from the asymptotic limits of the time of liquid–liquid phase separation, $\tau_{\text{LLPS}} \rightarrow \infty$, as shown in Fig. 10(a) for $q^* = 0.15$ and $T_c = 2.35$.

the underlying pressure dependence of the critical temperature of the liquid–liquid transition in the thermodynamic limit (T_c), at infinite k_d , due to the compressibility of the tetramer model. The values for the critical temperature for three different pressures are given in the caption of Fig. 11(a).

Rescaling the onset temperature by $T_c(P)$ gives the universal function of k_d depicted in Fig. 11(b). We also show in Fig. 11(b) the predictions of T^* obtained for three selected values of k_d through the asymptotic limits of $\tau_{\text{LLPS}} \rightarrow \infty$ as illustrated in Fig. 10(a). The predictions of T^* are just above the observed onset temperature because they correspond to slightly higher values of q^* and T_c (0.15 vs 0.11 and 2.35 vs 2.30, respectively). This difference can be attributed to uncertainty in obtaining the onset of phase separation on the scale of the simulation box. These values, however, are in good agreement with the computational T^* data obtained from the onset of phase separation.

As predicted from the growth rate factor, both conservative and dissipative force formulations will become identical in the limit of an infinitely rigid spring constant ($k_d \rightarrow \infty$) or when the kinetic interconversion Onsager coefficient goes to zero ($L \rightarrow 0$). We confirm this prediction by extrapolating the critical temperatures shown in Fig. 11(a) to $k_d \rightarrow \infty$ and comparing $T_c(P)$ to the ones obtained from the conservative force formulation. Remarkably, this pressure dependence of the critical temperature for the conservative-force formulation of the chiral model is fully consistent with the prediction obtained from the dissipative-force formulation as shown in Fig. 2. This is evidence for the consistency of our computational data for these two alternative formulations of the chiral model.

IV. CONCLUSION

The computational study of a three-dimensional off-lattice model of enantiomers with tunable chiral-interconversion kinetics reveals that arrested liquid–liquid phase separation into microdomains is observed when the intermolecular forces are not fully balanced, thus generating dissipation of energy, which converts this model into a nonequilibrium steady-state model. This imbalance acts as a racemizing force that causes the arrest of the phase domain growth. In the conserved formulation, when the forces are balanced, the phenomenon of phase amplification, when one phase grows at the expense of the other, emerges, and the phase domain growth is only restricted by the system size. From a numerical point of view, when the dihedral force constant k_d increases, the kinetics of interconversion slow down correspondingly, causing phase amplification to slow down and making it accordingly more difficult to observe the phenomenon on practical simulation times. In the limit of $k_d \rightarrow \infty$, the system would undergo the usual phase separation.⁵⁰

The physics driving amplification originates from the fact that molecules can interconvert, and “species” (in this case, molecules of types A and B) are not conserved. This provides the system with a mechanism for avoiding the energetically unfavorable formation of an interface between A-rich and B-rich phases, namely, by committing (randomly, of course) to one or the other choice.

This work can be extended to further investigate the role of the chiral bias parameter, λ , on interconversion and phase separation behavior. The tetramer model can also be generalized to

consider the nonzero enthalpy of interconversion where the interconversion rates for $A \rightarrow B$ and $B \rightarrow A$ could be different; thus, the equilibrium concentration of the enantiomers would be a function of temperature. Generalization of the approach developed here for the particular case of an interconvertible chiral model could significantly improve the fundamental understanding of the nature of phase behavior in a broad range of systems including polyamorphic liquids^{59,60} and nonequilibrium phase separation of proteins into microdomains.^{61–64} Examples of such possible generalizations include molecules whose local environment can fluctuate between (low-density, low-energy) and (high-density, high-energy) configurations (e.g., tetrahedral liquids, such as water or silicon), and proteins undergoing reversible structural fluctuations.

ACKNOWLEDGMENTS

We thank Sergey V. Buldyrev who suggested considering the forced interconversion through an imbalance of intermolecular forces and Nikolai D. Petsev for the development of the code for the conservative-force formulation of the chiral model. M.A.A. and P.G.D. acknowledge the financial support of the National Science Foundation (Award Nos. CHE-1856479 and CHE-1856704, respectively). Simulations were performed on computational resources managed and supported by Princeton Research Computing, a consortium of groups including the Princeton Institute for Computational Science and Engineering (PICSciE) and the Office of Information Technology's High Performance Computing Center and Visualization Laboratory at Princeton University.

DATA AVAILABILITY

The data that support the findings of this study are available from the corresponding author upon reasonable request.

APPENDIX A: MOLECULAR SIMULATION DETAILS

We conducted the simulations using a modified version of the molecular dynamics (MD) package Large-scale Atomic/Molecular Massively Parallel Simulator (LAMMPS) for the conservative force formulation.⁴⁹ The modified version takes into account the additional, multi-body forces⁴⁹ arising from the explicit chirality dependence of the interaction energy term in the intermolecular potential energy function [Eqs. (3) and (4)]. MD simulations were performed in an isothermal-isobaric ensemble. The temperature and pressure were controlled using Nosé–Hoover thermostats and barostats, respectively. Periodic boundary conditions were applied in three directions. The spherical cutoff for pair interactions was set to $3.5\sigma_{tt}$ for the energy-conserving model and $3\sigma_{tt}$ for the energy-dissipative model. A time step of $0.0005 t$ was used, in which t is time in reduced units.

APPENDIX B: THE PHASE DOMAIN GROWTH RATE

1. Conservative-force formulation of the chiral model

When a binary mixture of two non-interconverting species is quenched from a high temperature to a low temperature, below the critical point of demixing, and below the limit of compositional stability (spinodal curve), phase separation occurs through a process known as spinodal decomposition.⁵⁶ By accounting for the Ising-like

interconversion of alternative molecular states in the conservative-force formulation of the chiral model, Cahn–Hilliard's theory of spinodal decomposition may be generalized to describe the hybrid diffusion and Ising-like interconversion dynamics. Consequently, the fluctuations of the order parameter for both components of the hybrid dynamics are not local and characterized by the same correlation length. This is performed through the introduction of interconversion dynamics into the temporal evolution of the concentration of one of the enantiomer species, c_A , toward equilibrium. As a result, in the conservative-force formulation, the temporal evolution is described by

$$\frac{\partial \hat{c}_A}{\partial t} = M\nabla^2 \mu - L\mu, \quad (B1)$$

where M and L are the diffusion and interconversion Onsager kinetic coefficients, respectively, and μ is the chemical potential difference between the two alternative species A and B , $\mu = \mu_A - \mu_B$, where $\mu = 0$ in equilibrium. The reduced concentration of enantiomer species A , \hat{c}_A , is related to the physical concentration through $\hat{c}_A = 2(c_A - 1/2)$. In the case when the chirality renormalization parameter λ produces a bias toward homochiral ($\lambda > 0$) or heterochiral ($\lambda < 0$) interactions, the interconversion dynamics is described through the same chemical-potential difference, μ , as in the diffusion term of Eq. (B1). As a result, these two terms contain the same bulk and interfacial (nonlocal) contributions to the free energy. The chemical-potential difference is determined through a Landau–Ginzburg free energy functional of the form

$$F(\hat{c}_A) = \int \left(f_0(\hat{c}_A) + \frac{1}{2}R_0^2|\nabla \hat{c}_A|^2 \right) dV, \quad (B2)$$

where the first term represents the thermodynamic “bulk” free energy density and the second term represents the contribution to the total free energy due to concentration inhomogeneities. In the second term, R_0 is the characteristic length scale of intermolecular interactions adopted as the size of a tetramer molecule ($R_0 = 1$ in reduced units). In the symmetric binary-lattice (regular solution) model formulated in the mean field approximation,⁵⁹ f_0 can be expressed through the Gibbs energy of mixing, ΔG_{mix} , as

$$f_0 = \frac{\Delta G_{\text{mix}}}{kT} = [c_A \ln c_A + (1 - c_A) \ln(1 - c_A)] + ac_A(1 - c_A), \quad (B3)$$

where the term in brackets is the ideal entropy of mixing and the last term is the enthalpy of mixing. In the chiral model, $a \approx \rho\lambda$, where ρ is the dimensionless density and λ is the chiral bias parameter. Expanding f_0 in the vicinity of the critical point, where $T_c = a/2$ and $\hat{c}_A = 0$, in the lowest approximation $f_0 = (1/2)\Delta T_c^2\hat{c}_A^2$, where the reduced distance to the critical point $\Delta T = T/T_c - 1$. Therefore, the chemical potential is found from the variational derivative of the free energy functional with respect to the concentration of A-type enantiomers, as

$$\mu = \frac{\delta F}{\delta c_A} = \frac{\partial f_0}{\partial \hat{c}_A} - \nabla^2 \hat{c}_A \approx \Delta T \hat{c}_A - \nabla^2 \hat{c}_A. \quad (B4)$$

Substituting Eq. (B4) into Eq. (B1), the characteristic growth rate of the inhomogeneities, also referred to as the “amplification factor,”⁵⁶ may be analytically determined with the use of Fourier analysis to give

$$\omega(q) = -\Delta T(L + Mq^2)(1 - \xi^2 q^2), \quad (B5)$$

where ξ is the correlation length of concentration fluctuations; in the mean field approximation, $\xi^2 \propto 1/(-\Delta T)$.⁵⁷ In the absence of interconversion ($L = 0$), Eq. (B5) reduces to the classical Cahn–Hilliard theory of spinodal decomposition.⁵⁶

2. Dissipative-force formulation of the chiral model

In the dissipative-force formulation of the chiral model, a sink of energy arises due to an imbalance in intermolecular forces, which changes the chemical potential associated with the interconversion dynamics in the temporal evolution of the concentration, given by Eq. (B1). Specifically, the imbalance in intermolecular forces alters the Gibbs energy of mixing, $\Delta G_{\text{mix}} = \Delta H_{\text{mix}} - T\Delta S_{\text{mix}}$, by effectively canceling the enthalpy of mixing.⁵⁷ Therefore, in this formulation, the nonequilibrium free energy (\tilde{f}_0) is given by

$$\tilde{f}_0 = \frac{\Delta \tilde{G}_{\text{mix}}}{kT} = c_A \ln c_A + (1 - c_A) \ln(1 - c_A), \quad (\text{B6})$$

in which just the entropic contribution to the free energy remains. This result is a first order approximation valid only close to thermodynamic equilibrium.⁴⁵ Thus, the energy dissipation forces the system into a “racemized” homogeneous state, which competes with the temporal evolution of the concentration toward thermodynamic equilibrium. Expanding the nonequilibrium free energy in the vicinity of the critical point to first order, we obtain $\tilde{f}_0 \approx -(1/2)\hat{T}\hat{c}_A^2$, where $\hat{T} = T/T_c$. Therefore, since the imbalance in forces only affects the interconversion dynamics, the temporal evolution of the concentration of species A, Eq. (B1), is modified to include a nonequilibrium chemical potential, $\tilde{\mu} \approx -\hat{T}\hat{c}_A - \nabla^2 \hat{c}_A$, and as such is given by

$$\frac{\partial \hat{c}_A}{\partial t} = M\nabla^2 \mu - L\tilde{\mu}, \quad (\text{B7})$$

where the first term is the equilibrium diffusion dynamics, unaffected by the imbalance in forces, and the second term is the nonequilibrium interconversion dynamics. The Fourier analysis of Eq. (B7) gives the growth rate for the dissipative-force formulation of the chiral system in the form

$$\tilde{\omega}(q) = -L\hat{T} - (M\Delta T + L)q^2 - Mq^4, \quad (\text{B8})$$

which is an alternative form of Eq. (11), given in the main text, through the use of the mean field correlation length, $\xi^2 = -1/\Delta T$.⁵⁷

APPENDIX C: DEPENDENCE OF PAIR INTERACTION ENERGY ON DIHEDRAL FORCE CONSTANT

Dependence of the total pair interaction energy on the dihedral force constant for the chiral model with conservative intermolecular forces at $k_d = 0.01$ (blue) and $k_d = 30$ (orange) (Fig. 13).

APPENDIX D: STRUCTURE FACTOR AND DOMAIN SIZE TEMPORAL EVOLUTION

The domain growth is determined through the time-dependent structure factor for the chiral system, $S(q, t)$. It is well-known that the classical Cahn–Hilliard theory is only valid for the early stages of spinodal decomposition.⁶⁵ To accurately describe the behavior of systems in the late stages of spinodal decomposition, and eventually, the crossover into the coarsening regime, as reported by

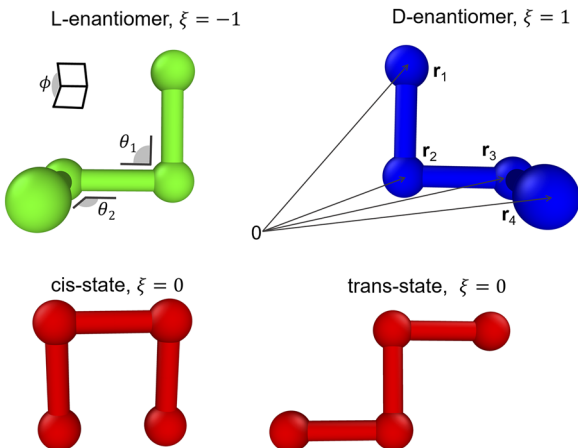


FIG. 12. Molecular representation and relevant geometrical features of tetramer molecules. Molecules exist in left-handed (A-type, green), right-handed (B-type, blue), or achiral (*cis*- or *trans*-, red) configurations.

Langer *et al.*⁶⁶ and Binder *et al.*,⁶⁷ two key alterations must be made to Cahn–Hilliard theory. First, concentration fluctuations, in the Ornstein–Zernike approximation,⁶⁷ are introduced into the time-dependent structure factor,⁶⁸ and second, the inverse susceptibility, $\partial^2 f_0 / \partial c_A^2$, must go to zero when the system reaches the spinodal. Adopting these changes into the time-dependent structure factor gives

$$S(q, t) = \frac{Mq^2 + L}{-\tilde{\omega}(q)} \left(1 - e^{2\tilde{\omega}(q)t} \right), \quad (\text{D1})$$

where ΔT in $\tilde{\omega}$, given by Eq. (B8), becomes time dependent and is represented as

$$\Delta T(t) = \Delta T(t=0)e^{-t/\tau}, \quad (\text{D2})$$

in which τ is a parameter that determines the transition from the early stages of spinodal decomposition to the coarsening regime.

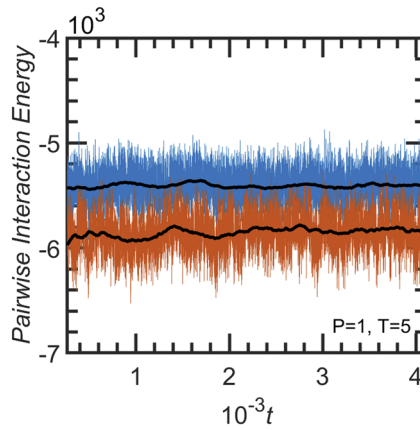


FIG. 13. Dependence of the total pair interaction energy on the dihedral force constant for the chiral model with conservative intermolecular forces at $k_d = 0.01$ (blue) and $k_d = 30$ (orange). The system consists of 1000 tetramers at $T = 5$, $P = 1$, and $\langle EE \rangle = 0$. The black lines are moving averages over time windows of duration $t = 200$.

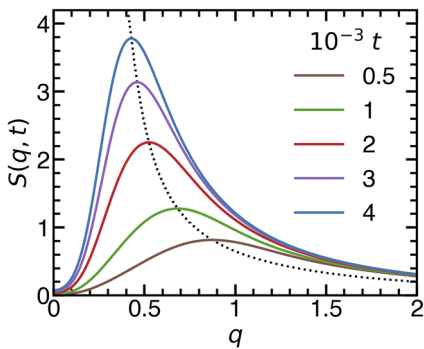


FIG. 14. Structure factor as given by Eq. (D1) for $T = 0.8$, $T_c = 2.32$, $k_d = 9.86$, $P = 0.1$, $\tau = 1100$, M given by the Einstein–Stokes relation, with $T_0 = 1.2$ and amplitude coefficient $b = 10^{-3}$, and L given by Eq. (10). Over time the maximum of $S(q, t)$, indicated by the dotted line, shifts to the left until $q_m \propto q_-$, but even in the $t \rightarrow \infty$ limit, the maximum never reaches zero wavenumber, thus corresponding to the formation of steady-state microdomains.

The domain size is determined from the characteristic wavenumber which corresponds to the maximum of the time-dependent structure factor. For instance, Fig. 14 shows the time evolution of the structure factor corresponding to $k_d = 9.86$ (whose time-dependent domain size is shown in Fig. 7). As illustrated, the maximum moves to the left until $q_m \propto q_-$, and if continued into the steady-state limit (when $t \rightarrow \infty$) the structure factor will never shift to zero wavenumber, indicating the formation of steady-state microdomains. The time evolution of the domain size [as presented in Figs. 7(a) and 7(b)] was determined from numerically calculating the time-dependent wave number corresponding to the maximum of the structure factor.⁵⁷

APPENDIX E: CHARACTERISTIC TIME SCALES IN THE DISSIPATIVE-FORCE FORMULATION OF THE CHIRAL MODEL

The characteristic time of liquid–liquid phase separation (τ_{LLPS}), interconversion (τ_{INC}), and molecular self-diffusion (τ_D) is well described through the generalized Cahn–Hilliard theory. The interconversion Onsager kinetic coefficient, L , is given through an extended version of Eq. (10) (given in the main manuscript) of the form

$$L = \frac{1}{\tau_{\text{INC}}} = bM(T_0, T) \frac{T^2}{k_d^2} \left(1 + c \frac{T^2}{k_d^2} \right), \quad (\text{E1})$$

in which b and c are constants. The mobility, M , is given through the Stokes–Einstein relation that $M = kT/6\pi\eta R_0$, where the viscosity of the system is assumed to be $\eta = e^{T_0/T}$, in which the characteristic temperature, T_0 , was also adjusted to better describe the behavior of each dihedral constant, k_d , at low temperatures.

The characteristic time of liquid–liquid phase separation (LLPS) in the dissipative-force formulation of the chiral model can be determined from the region where $q_- < q^*$. In this region, the finite size of the system limits the size of the microdomains that may form, which is computationally observed as “complete” phase separation. Therefore, the characteristic LLPS time is found as $\tau_{\text{LLPS}} = a_{\text{LLPS}}/\tilde{\omega}(q^*)$, where the amplitude $a_{\text{LLPS}} = 0.34$ and $T_c = 2.35$. In the fit, presented in Fig. 10(a), q^* is adjusted such that $\tau_{\text{LLPS}} \rightarrow \infty$

when the temperature reaches T^* , the onset of phase separation on the scale of the simulation box. In addition, the characteristic temperature T_0 was slightly different for the three different dihedral constants: $T_0 = 2.2(k_d = 5)$, $T_0 = 1.925(k_d = 9.86)$, and $T_0 = 1.2(k_d = 19.86)$.

The characteristic interconversion time, τ_{INC} , of a tetramer is shown in Fig. 10(b). It is described by Eq. (E1), for which the constants were found to be $T_0 = 0.36$, $b = 29.4$, and $c = 526.6$.

Equation (B8) introduces an effective molecular self-diffusion coefficient, by the slope of the amplification factor at small wave numbers, which modifies the growth of the phase domain. This property is given by the coefficient of the q^2 term in Eq. (B8), which reads as $D_{\text{eff}} = (M\Delta T + L)/\hat{T}$. As a result, the characteristic time of molecular self-diffusion [Fig. 10(c)] is found from $\tau_D = a_D/D_{\text{eff}}$, where a_D is an amplitude coefficient of the order R_0^2 , determined from the fit to be 0.94. In addition, the characteristic temperature T_0 was found to be somewhat different for the three different dihedral constants: $T_0 = 3.4(k_d = 5)$, $T_0 = 4.8(k_d = 9.86)$, and $T_0 = 7.0(k_d = 19.86)$.

REFERENCES

- ¹ Chirality in Natural and Applied Science, edited by W. J. Lough and I. W. Wainer (Blackwell Science, Oxford, UK, 2002).
- ² V. A. Guijarro and M. Yus, *The Origin of Chirality in the Molecules of Life* (The Royal Society, Cambridge, UK, 2009).
- ³ L. D. Barron, *Origins Life Evol. Biospheres* **44**, 61 (2014).
- ⁴ K. Hoehlig, L. Bethge, and S. Klussmann, *PLoS One* **10**, e0115328 (2015).
- ⁵ A. N. Collins, G. N. Sheldrake, and J. Crosby, *J. Chem. Educ.* **70**, A199 (1993).
- ⁶ H.-U. Blaser, *Rendi. Lincei* **24**, 213 (2013).
- ⁷ H.-U. Blaser, *Rendi. Lincei* **18**, 281 (2007).
- ⁸ G.-Q. Lin, J.-G. Zhang, and J.-F. Cheng, *Chiral Drugs* (John Wiley & Sons, 2011), pp. 3–28.
- ⁹ G. Yang and H.-Z. Bu, *Chiral Drugs* (John Wiley & Sons, 2011), pp. 381–399.
- ¹⁰ N. Chhabra, M. Aseri, and D. Padmanabhan, *Int. J. Appl. Basic Med. Res.* **3**, 16 (2013).
- ¹¹ J. Govan and Y. K. Gun’ko, *Nanoscience* (Royal Society of Chemistry, 2016), pp. 1–30.
- ¹² A. O. Govorov, Y. K. Gun’ko, J. M. Slocik, V. A. Gérard, Z. Fan, and R. R. Naik, *J. Mater. Chem.* **21**, 16806 (2011).
- ¹³ A. Guerrero-Martínez, J. L. Alonso-Gómez, B. Auguié, M. M. Cid, and L. M. Liz-Marzán, *Nano Today* **6**, 381 (2011).
- ¹⁴ R. Breslow, *Tetrahedron Lett.* **52**, 2028 (2011).
- ¹⁵ D. K. Kondepudi and G. W. Nelson, *Nature* **314**, 438 (1985).
- ¹⁶ F. C. Frank, *Biochim. Biophys. Acta* **11**, 459 (1953).
- ¹⁷ K. Soai, T. Shibata, H. Morioka, and K. Cho, *Nature* **378**, 767 (1995).
- ¹⁸ T. Shibata, H. Morioka, T. Hayase, K. Cho, and K. Soai, *J. Am. Chem. Soc.* **118**, 471 (1996).
- ¹⁹ G. Lente, *Phys. Chem. Chem. Phys.* **9**, 6134 (2007).
- ²⁰ H. W. Hatch, F. H. Stillinger, and P. G. Debenedetti, *J. Chem. Phys.* **133**, 224502 (2010).
- ²¹ F. Ricci, F. H. Stillinger, and P. G. Debenedetti, *J. Phys. Chem. B* **117**, 602 (2013).
- ²² T. G. Lombardo, F. H. Stillinger, and P. G. Debenedetti, *Proc. Natl. Acad. Sci. U. S. A.* **106**, 15131 (2009).
- ²³ M. Cao and P. A. Monson, *J. Chem. Phys.* **122**, 054505 (2005).
- ²⁴ F. H. Stillinger, *J. Phys. Chem. B* **122**, 3441 (2017).
- ²⁵ S. F. Mason and G. E. Tranter, *Proc. R. Soc. London, Ser. A* **397**, 45 (1985).
- ²⁶ J. L. Bada, *Nature* **374**, 594 (1995).
- ²⁷ P. G. H. Sandars, *Origins Life Evol. Biospheres* **33**, 575 (2003).
- ²⁸ D. G. Blackmond, *Proc. Natl. Acad. Sci. U. S. A.* **101**, 5732 (2004).
- ²⁹ D. G. Blackmond, *Cold Spring Harbor Perspect. Biol.* **101**, a032540 (2019).

- ³⁰W. L. Noorduin, T. Izumi, A. Millemaggi, M. Leeman, H. Meekes, W. J. P. Van Enckevort, R. M. Kellogg, B. Kaptein, E. Vlieg, and D. G. Blackmond, *J. Am. Chem. Soc.* **130**, 1158 (2008).
- ³¹G. Laurent, D. Lacoste, and P. Gaspard, *Proc. Natl. Acad. Sci. U. S. A.* **118**, e2012741118 (2021).
- ³²F. Jafarpour, T. Biancalani, and N. Goldenfeld, *Phys. Rev. Lett.* **115**, 158101 (2015).
- ³³F. Jafarpour, T. Biancalani, and N. Goldenfeld, *Phys. Rev. E* **95**, 032407 (2017).
- ³⁴D. Sutton, J. L. Stanford, and A. J. Ryan, *J. Macromol. Sci. Phys.* **43**, 233 (2004).
- ³⁵G. Zhang, G. Liu, Z. Shi, and G. Qiao, *RSC Adv.* **4**, 7068 (2014).
- ³⁶I. A. Zucchi, M. J. Galante, J. Borrajo, and R. J. J. Williams, *Macromol. Chem. Phys.* **205**, 676 (2004).
- ³⁷R. J. J. Williams, B. A. Rozenberg, and J.-P. Pascault, "Reaction-induced phase separation in modified thermosetting polymers," in *Polymer Analysis Polymer Physics* (Springer, Berlin, Heidelberg, 1997), pp. 95–156.
- ³⁸K.-W. D. Lee, P. K. Chan, and X. Feng, *Macromol. Theory Simul.* **12**, 413 (2003).
- ³⁹K. Kataoka, O. Urakawa, H. Nishioka, and Q. Tran-Cong, *Macromolecules* **31**, 8809 (1998).
- ⁴⁰A. Harada and Q. Tran-Cong, *Macromolecules* **29**, 4801 (1996).
- ⁴¹Q. Tran-Cong, T. Ohta, and O. Urakawa, *Phys. Rev. E* **56**, R59 (1997).
- ⁴²Q. Tran-Cong, J. Kawai, Y. Nishikawa, and H. Jinna, *Phys. Rev. E* **60**, R1150 (1999).
- ⁴³S. C. Glotzer, D. Stauffer, and N. Jan, *Phys. Rev. Lett.* **72**, 4109 (1994).
- ⁴⁴S. C. Glotzer, E. A. Di Marzio, and M. Muthukumar, *Phys. Rev. Lett.* **74**, 2034 (1995).
- ⁴⁵A. Lamorgese and R. Mauri, *Phys. Rev. E* **94**, 022605 (2016).
- ⁴⁶R. Lefever, D. Carati, and N. Hassani, *Phys. Rev. Lett.* **75**, 1674 (1995).
- ⁴⁷D. Carati and R. Lefever, *Phys. Rev. E* **56**, 3127 (1997).
- ⁴⁸F. Latinwo, F. H. Stillinger, and P. G. Debenedetti, *J. Chem. Phys.* **145**, 154503 (2016).
- ⁴⁹N. D. Petsev, F. H. Stillinger, and P. G. Debenedetti, *J. Chem. Phys.* **155**, 084105 (2021).
- ⁵⁰N. A. Shumovskyi, T. J. Longo, S. V. Buldyrev, and M. A. Anisimov, *Phys. Rev. E* **103**, L060101 (2021).
- ⁵¹R. Ball and J. Brindley, *Origins Life Evol. Biospheres* **46**, 81 (2015).
- ⁵²S. C. Abrahams, R. L. Collin, and W. N. Lipscomb, *Acta Crystallogr.* **4**, 15 (1951).
- ⁵³W. R. Busing and H. A. Levy, *J. Chem. Phys.* **42**, 3054 (1965).
- ⁵⁴C. Viedma, *Origins Life Evol. Biosphere* **31**, 501 (2001).
- ⁵⁵H. N. Bordallo, B. A. Kolesov, E. V. Boldyrev, and F. Juranyi, *J. Am. Chem. Soc.* **129**, 10984 (2007).
- ⁵⁶J. W. Cahn, *J. Chem. Phys.* **42**, 93 (1965).
- ⁵⁷T. J. Longo and M. A. Anisimov, *arXiv:2102.11148v4* (2021).
- ⁵⁸J. W. Cahn and J. E. Hilliard, *J. Chem. Phys.* **28**, 258 (1958).
- ⁵⁹M. A. Anisimov, M. Duška, F. Caupin, L. E. Amrhein, A. Rosenbaum, and R. J. Sadus, *Phys. Rev. X* **8**, 011004 (2018).
- ⁶⁰K. Takae and H. Tanaka, *Proc. Natl. Acad. Sci. U. S. A.* **117**, 4471 (2020).
- ⁶¹A. A. Hyman, C. A. Weber, and F. Jülicher, *Annu. Rev. Cell Dev. Biol.* **30**, 39 (2014).
- ⁶²Y. Shin and C. P. Brangwynne, *Science* **357**, eaaf4382 (2017).
- ⁶³M.-T. Wei, S. Elbaum-Garfinkle, A. S. Holehouse, C. C.-H. Chen, M. Feric, C. B. Arnold, R. D. Priestley, R. V. Pappu, and C. P. Brangwynne, *Nat. Chem.* **9**, 1118 (2017).
- ⁶⁴S. Ranganathan and E. Shakhnovich, *eLife* **9**, e56159 (2020).
- ⁶⁵J. W. Cahn, *Acta Metall.* **14**, 1685 (1966).
- ⁶⁶J. S. Langer, M. Bar-on, and H. D. Miller, *Phys. Rev. A* **11**, 1417 (1975).
- ⁶⁷K. Binder, C. Billotet, and P. Mirold, *Z. Phys. B: Condens. Matter* **30**, 183 (1978).
- ⁶⁸H. E. Cook, *Acta Metall.* **18**, 297 (1970).